

Transport through quantum dots: A combined DMRG and cluster-embedding study

F. Heidrich-Meisner

Materials Science and Technology Division, Oak Ridge National Laboratory, Oak Ridge, Tennessee 37831, USA and
Department of Physics and Astronomy, University of Tennessee, Knoxville, Tennessee 37996, USA

G.B. Martins

Department of Physics, Oakland University, Rochester, Michigan 48309, USA

C.A. Büsser

Department of Physics and Astronomy, Ohio University, Athens, Ohio 45701, USA

K.A. Al-Hassanieh

Materials Science and Technology Division, Oak Ridge National Laboratory, Oak Ridge, Tennessee 37831, USA and
Department of Physics and Astronomy, University of Tennessee, Knoxville, Tennessee 37996, USA
National High Magnetic Field Laboratory and Department of Physics, Florida State University, Tallahassee, Florida 32306, USA

A.E. Feiguin

Microsoft Project Q, University of California, Santa Barbara, CA 93106, USA

G. Chiappe

Departamento de Física J.J. Giambiagi, Facultad de Ciencias Exactas, Universidad de Buenos Aires, Ciudad Universitaria, 1428 Buenos Aires, Argentina.
Departamento de Física Aplicada, Unidad Asociada del Consejo Superior de Investigaciones Científicas and Instituto Universitario de Materiales, Universidad de Alicante, San Vicente del Raspeig, Alicante 03690, Spain.

E.V. Anda

Departamento de Física, Pontificia Universidade Católica do Rio de Janeiro (PUC-Rio), 22452-970, Caixa Postal: 38071 Rio de Janeiro, Brazil.

E. Dagotto

Materials Science and Technology Division, Oak Ridge National Laboratory, Oak Ridge, Tennessee 37831, USA and

Department of Physics and Astronomy, University of Tennessee, Knoxville, Tennessee
37996, USA

E-mail: `fabian.heidrich-meisner@physik.rwth-aachen.de`

Abstract. The numerical analysis of strongly interacting nanostructures, such as quantum dots, requires powerful techniques. Recently developed methods, such as the time-dependent density matrix renormalization group approach or the embedded-cluster approximation, rely on the numerical solution of clusters of finite-size. For the interpretation of numerical results, it is therefore crucial to understand finite-size effects in detail. In this work, we present a careful finite-size analysis for the examples of one quantum dot, as well as three serially connected quantum dots. Depending on “odd-even” effects, physically quite different results may emerge from clusters that do not differ much in their size. The insights of this study also provide a solution to a recent controversy over results obtained with the embedded-cluster method for the case of three quantum dots. In particular, using the optimum clusters discussed in this paper, the parameter range in which the embedded-cluster approach can reliably be applied is increased, as we show for the case of three quantum dots. As a practical procedure, we propose that a comparison of results for static quantities against those of quasi-exact methods, such as DMRG, serves to identify the optimum cluster type. In the examples studied here, we find that to observe signatures of the Kondo effect in finite systems, the best clusters involving dots and leads must have a total z -component of the spin equal to zero.

PACS numbers: 73.23.Hk, 72.15.Qm, 73.63.Kv

The prediction and experimental observation of the Kondo effect in quantum dots [1, 2, 3, 4] and single-molecule conductors has stimulated considerable interest in strongly correlated nano-scale systems, as discussed in recent reviews [5, 6, 7]. The related experimental and theoretical efforts are not only motivated by novel emerging physical phenomena, but also by the possible technological applications of nanodevices, and in particular by their transport properties. Experimental results for the conductance through nanostructures have been reported for single dots, side and linearly coupled two dots, as well as small molecules [1, 8, 9].

Stimulated by the rich physics harbored by interacting nanostructures, the field has seen a rapid development of powerful numerical techniques. These include the well-established numerical-renormalization group approach (NRG) [10, 11, 12], the recently developed time-dependent density-matrix renormalization group (tDMRG) method [13, 14, 15, 16, 17, 18, 19, 20] functional renormalization group approaches [21] as well as exact diagonalization combined with an embedding procedure (ECA) [22, 23, 24, 25, 26].

Time-dependent DMRG and ECA are particularly promising methods to address complex nanoscale systems such as molecular conductors. Both methods can include the modeling of phonons. As both DMRG and ECA are based on real-space schemes, for the interpretation of numerical results, it is crucial to understand how subtle many-body effects, such as the Kondo effect, manifest themselves on finite systems. It is one of the advantages of DMRG and ECA that spatial correlations can be analyzed not only within the interacting region, but also throughout the entire system. Therefore, it is possible to study how the screening of the magnetic moment of quantum dots occurs on finite systems, which relates to the notion of the so-called *Kondo cloud* [27, 28, 29, 30]. The computation of extended spatial correlations within NRG has become possible only recently [31].

It is the purpose of this work to present a detailed analysis of the properties of strongly interacting nanostructures and their finite-size scaling, in both DMRG and ECA calculations. Our manuscript first provides a discussion of the one-dot case and then covers three serially coupled quantum dots as well. The models are schematically depicted in Fig. 1.

We discuss how the emergence of Kondo physics – or its absence – is reflected in static properties, such as spin and charge fluctuations and spin-spin correlations. In addition, we discuss the conductance of these structures as a function of model parameters and gate voltage, which controls the dots’ filling. As our main result, we argue that, in certain cases, it is important to consider the geometric properties and global quantum numbers of finite systems in order to correctly interpret the results from exact diagonalization (ED)-based approaches such as ECA. The main conclusions are relevant for real-time simulations within tDMRG as well.

The case of three dots [21, 24, 25, 32, 33, 34, 35, 36, 37, 38] has attracted considerable attention from the theoretical side. Most studies find perfect conductance through the dots at half filling, independently of model parameters such as hopping

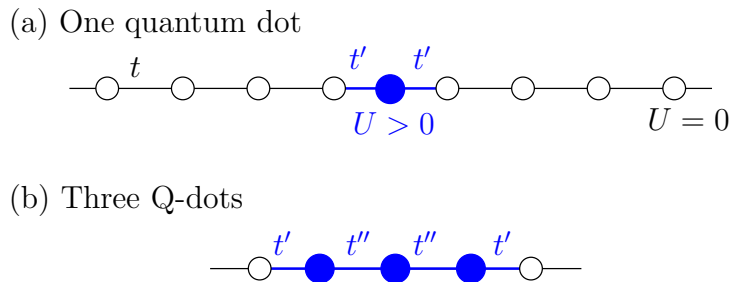


Figure 1. Sketch of the models studied in this work: (a) a single quantum dot embedded into noninteracting leads; (b) three serially coupled dots embedded into leads. Full symbols denote dots (namely, sites with a finite onsite Coulomb repulsion $U > 0$), while open symbols represent tight-binding sites.

matrix elements between the dots and onsite Coulomb repulsion [21, 32, 34, 35, 36, 37]. This result is at odds with earlier results obtained from ECA since a conductance dip has been reported in Ref. [25]. Here, we resolve this issue and show that, unlike some claims in the literature, the controversial dip is not due to an incapability of ECA to capture the essential physics, but due to quite subtle finite-size effects which have not been appreciated in detail before.

The ECA method incorporates the numerical solution of a small cluster that contains the interacting region – e.g., a quantum dot – by means of exact diagonalization. One example of a relevant global quantum number of such small clusters is S_{total}^z , the z -component of the total spin. We show that in certain cases, clusters with an overall $S_{\text{total}}^z \neq 0$ and open boundary conditions may exhibit qualitatively different properties from those with $S_{\text{total}}^z = 0$. Furthermore, as a practical procedure, we propose that a quantitative comparison of static properties, such as charge variations with gate potential, between ECA and DMRG would allow us to determine the optimum cluster-type for a given model.

The Hamiltonian consists of three parts: the noninteracting leads H_{leads} , the coupling between the interacting region and the leads, H_{hy} , and the interacting region described by H_{int} :

$$H = H_{\text{leads}} + H_{\text{int}} + H_{\text{hy}}, \quad (1)$$

where the leads are described by:

$$H_{\text{leads}} = -t \sum_{l=1}^{N_L-1} [c_{l,\sigma}^\dagger c_{l+1,\sigma} + \text{H.c.}] - t \sum_{l=N_L+N_{\text{int}}+1}^{N-1} [c_{l,\sigma}^\dagger c_{l+1,\sigma} + \text{H.c.}]. \quad (2)$$

As usual, $c_{l,\sigma}^{(\dagger)}$ denotes a fermion annihilation (creation) operator acting on site l , with a spin index $\sigma = \uparrow, \downarrow$. Summation over a repeated index σ is implied throughout the paper. $n_{l,\sigma} = c_{l,\sigma}^\dagger c_{l,\sigma}$ is the local particle operator with spin σ and $n_l = n_{l,\uparrow} + n_{l,\downarrow}$ is the particle number (or charge) operator on site l . The total system size is $N = N_L + N_{\text{int}} + N_R$, where $N_{L(R)}$ is the number of sites in the left(right) lead and N_{int} is the number of interacting sites in the center of the system. The hybridization

term can be written as:

$$H_{\text{hy}} = -t' \sum_{\sigma} (c_{N_L, \sigma}^{\dagger} c_{N_L+1, \sigma} + c_{x, \sigma}^{\dagger} c_{x+1, \sigma} + \text{H.c.}), \quad (3)$$

with $x = N_L + N_{\text{int}}$. Unless otherwise stated, $t = 1$ is the unit of energy. The quantum of conductance in this notation is thus $G_0 = 1$ (for one spin channel).

The rest of the paper is organized as follows. In Sec. 1, we introduce the two methods used here, DMRG and ECA. In Sec. 2, we revisit the case of a single quantum dot. We point out that tDMRG calculations result in quite different behaviors, depending on the type of open clusters. We qualitatively discuss spin-spin correlations to analyze impurity screening and calculate the conductance as a function of gate voltage with ECA. In Sec. 3, we present our numerical results for static properties of three quantum dots obtained from DMRG calculations, with a special focus on their finite-size dependence. This allows us to identify the optimum clusters for the calculation of dynamic properties and the conductance. Section 4 provides a summary and conclusions.

1. Methods

1.1. DMRG

The set-up for time-dependent DMRG calculations of transport properties has been detailed in Ref. [19]. Here we just repeat that the current $J(\tau)$ [where τ denotes time] is measured as the current across the link between the leads and the interacting region [see Eq. (3)]:

$$j_{x, x+1} = -it'(c_{x+1}^{\dagger} c_x - \text{H.c.}); \quad J = \langle j_{x, x+1} \rangle \quad (4)$$

with $x = N_L + N_{\text{int}}$ or $x = N_L$. The external bias – an onsite potential $\pm \Delta V n_i$ applied to the leads – is $\Delta V \sim 10^{-3}$. We use a Trotter-Suzuki break-up of the time evolution operator in our adaptive tDMRG scheme with a time step of $\delta\tau \sim 0.01$ [15, 16]. The truncation error during the time evolution is kept below 10^{-8} . Open boundary conditions are imposed in all DMRG calculations.

1.2. ECA

The ECA method relies – similarly to DMRG – on the numerical determination of the ground-state of a cluster with open boundary conditions. We only briefly sketch the method here, while a detailed description can be found in Refs. [22, 23, 24, 39].

The ECA method tackles the impurity problem in three steps. First, the infinite system is artificially cut into two parts: one part **C** that contains the interacting region plus as many noninteracting sites of the leads as possible (this part will, from now on, be referred to as ‘the cluster’), and a second part **R** (the ‘rest’), consisting of semi-infinite chains positioned at left and right in relation to the cluster **C**. The number of sites in **C** is denoted by N_{ED} . Second, Green’s functions (GF) for both parts are computed independently: current implementations of ECA utilize the Lanczos method

to calculate the interacting region's GF, while those of the part \mathbf{R} , being noninteracting, can be computed exactly as well. In a final step, the artificially disconnected parts are reconnected by means of a Dyson equation, which dresses the interacting region's GF. This step, the actual embedding, is crucial for capturing the many-body physics associated with the Kondo effect. Moreover, although the clusters that can be solved exactly by means of a Lanczos routine are rather small, being of the order of $N_{\text{ED}} \approx 12$ sites only, the embedding step largely compensates for that by dressing the cluster GF and effectively extending the many-body correlations, induced by the presence of the impurity, into the semi-infinite chains \mathbf{R} .

We now further detail these steps. The Hamiltonians of the left and right semi-infinite, tight-binding chains, i.e., the noninteracting \mathbf{R} part, are described by

$$H_{\text{sc-L}} = -t \sum_{l=0,\sigma}^{-\infty} (c_{l\sigma}^\dagger c_{l-1\sigma} + h.c.); \quad H_{\text{sc-R}} = -t \sum_{l=N_{\text{ED}}+1,\sigma}^{\infty} (c_{l\sigma}^\dagger c_{l+1\sigma} + h.c.), \quad (5)$$

where in this notation, the sites labeled by $i = 1, \dots, N_{\text{ED}}$ are inside the cluster \mathbf{C} . The semi-infinite chains are connected to the cluster by the following term:

$$H_{\text{hy}} = -t [c_{1\sigma}^\dagger c_{0\sigma} + c_{N_{\text{ED}}\sigma}^\dagger c_{N_{\text{ED}}+1\sigma}] + h.c.. \quad (6)$$

The GF for the cluster \mathbf{C} and for the semi-infinite chains are calculated at zero temperature. Fixing the number of particles m and the z -axis projection of the total spin, S_{total}^z , the ground state and the one-body propagators between all the clusters' sites are calculated. These GFs can be written as an $N_{\text{ED}} \times N_{\text{ED}}$ matrix $\hat{G}_c^{(m, S_{\text{total}}^z)}$, where the row and column indexes run over the cluster's sites. For the noninteracting, semi-infinite chains, the GFs G_0 and $G_{N_{\text{ED}}+1}$ at the sites 0 and $N_{\text{ED}}+1$, located at the extreme ends of the semi-infinite chains adjacent to the cluster, can easily be calculated as well. In order to write the Dyson equation in matrix form, GF matrices \hat{G}_r for each semi-infinite chain are defined, which have the same dimension as $\hat{G}_c^{(m, S_{\text{total}}^z)}$, representing the contribution of the sites '0' and ' $N_{\text{ED}}+1$ ' to the dressing of the cluster GF $\hat{G}_c^{(m, S_{\text{total}}^z)}$. All matrix elements vanish, except for the diagonal matrix elements corresponding to sites '0' and ' $N_{\text{ED}}+1$ ', which take the values calculated for G_0 and $G_{N_{\text{ED}}+1}$. A generalized notation \hat{G}_r will be used for the semi-infinite chains' GF matrices, where 'r' stands for either 'Lsc' or 'Rsc', i.e, the left and right semi-infinite chains, respectively.

The Dyson equation used to calculate the dressed GF matrix elements $\hat{G}_T^{i,j}$, can therefore be written as

$$\hat{G}_{T \ c,c}^{(m, S_{\text{total}}^z)} = \hat{G}_c^{(m, S_{\text{total}}^z)} + \sum_r \hat{G}_c^{(m, S_{\text{total}}^z)} \hat{T}_{\mathbf{c},\mathbf{r}} \hat{G}_{T \ r,c}^{(m, S_{\text{total}}^z)} \quad (7)$$

$$\hat{G}_{T \ r,c}^{(m, S_{\text{total}}^z)} = \hat{G}_r \delta_{rc} + \hat{G}_r \hat{T}_{\mathbf{c},\mathbf{r}}^t \hat{G}_{T \ c,c}^{(m, S_{\text{total}}^z)}, \quad (8)$$

where $\hat{T}_{\mathbf{c},\mathbf{r}}$, also an $N_{\text{ED}} \times N_{\text{ED}}$ matrix, connects the cluster \mathbf{C} to the rest of the system, and is defined according to H_{hy} . $\hat{G}_{T \ i,j}^{(m, S_{\text{total}}^z)}$ is the propagagator for an electron moving from site i to site j , where we put $i = c$ if i is in the cluster and $i = r$, if i is in the rest of the system. Eqs. (7) and (8) correspond to a chain approximation, where a

locator-propagator diagrammatic expansion is used [40, 41]. Note that ECA is exact in the case of $U = 0$, i.e., noninteracting quantum dots.

As mentioned before, the calculation of the propagator $\hat{G}_c^{(m, S_{\text{total}}^z)}$ requires that fixed quantum numbers m and S_{total}^z be used. However, after dressing with \hat{G}_r , these quantum numbers are not good quantum numbers for the cluster anymore. Therefore, we have to incorporate processes into the ECA method that allow for charge fluctuations in the cluster \mathbf{C} . To accommodate this requirement, different implementations of ECA have been devised, either by including different spin mixing strategies [22, 42, 43, 44] or by moving the Fermi energy of the leads [45, 46]. A survey over these different implementations is in preparation [26].

For this work, we will adopt a ‘spin mixing’ strategy different from the one used in a previous work analyzing the three-dots geometry [25]. We will show that this different strategy is instrumental in decreasing finite-size effects observed in Ref. [25]. The spin mixing proceeds as follows. First, a cluster GF with mixed charge, but fixed spin, is defined through

$$\hat{G}_c^{(m+p, pS_{\text{total}}^z)} = (1-p) \hat{G}_c^{(m, 0)} + p \hat{G}_c^{(m+1, S_{\text{total}}^z)}, \quad (9)$$

where p takes values between 0 and 1, and we are assuming that m is even, in which case, the corresponding $S_{\text{total}}^z = 0$. In addition, note that for the cluster with charge $m+1$, S_{total}^z takes values $\pm 1/2$. The matrix $\hat{G}_c^{(m+p, pS_{\text{total}}^z)}$ corresponds to a situation where the charge in the cluster is between m and $m+1$. The total charge in the cluster, before embedding, can easily be calculated as

$$q^{pS_{\text{total}}^z}(p) = (1-p)m + p(m+1) = m+p. \quad (10)$$

Using Eqs. (7) and (8), the dressed GF $\hat{G}_T^{(m+p, pS_{\text{total}}^z)}$ is obtained, and from this result, the charge in the cluster can be calculated:

$$Q^{pS_{\text{total}}^z}(p) = \frac{-1}{\pi} \int_{-\infty}^{E_F} \text{Im } \text{tr} \{ \hat{G}_T^{(m+p, pS_{\text{total}}^z)}(\omega) \} d\omega, \quad (11)$$

where E_F is the Fermi level. The value of p is calculated self-consistently, satisfying

$$Q^{pS_{\text{total}}^z}(p) = q^{pS_{\text{total}}^z}(p). \quad (12)$$

If there is spin reversal symmetry, e.g., no magnetic field is applied, one can calculate the total GF as

$$\hat{G}_T(p) = \frac{1}{2} \sum_{S_{\text{total}}^z = \pm 1/2} \hat{G}_T^{(m+p, pS_{\text{total}}^z)}, \quad (13)$$

where p satisfies Eq. (12). It is important to emphasize that the charge fluctuations taken into account by Eq. (12) are the ones between the cluster and the rest of the system, and not just the ones at the interacting region described by H_{int} . The latter ones involve a very localized neighborhood of the dot and as a consequence, are typically already well described on isolated clusters only.

As will be shown in Sec. 3.2, this alternative way of obtaining the dressed GF leads to improved results in the case of three dots. Note that in the case of one dot,

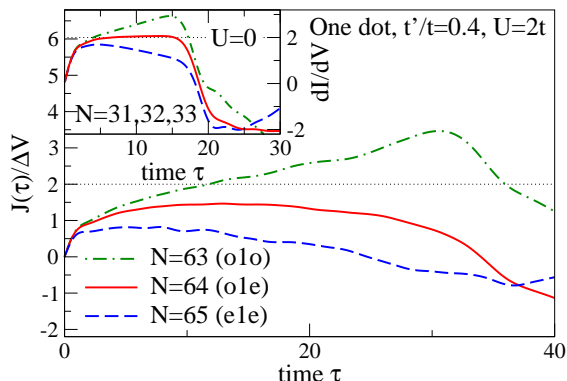


Figure 2. One dot, $t'/t = 0.4$, $V_g = -U/2$. Main panel: current $J(\tau)/\Delta V$ vs. time for $N = 63$ ($o1o$), $N = 64$ ($o1e$), and $N = 65$ ($e1e$) at $U/t = 2$ (DMRG, bias $\Delta V = 0.005$). Inset: current $J(\tau)/\Delta V$ vs. time at $U = 0$ for $N = 31, 32, 33$ (exact diagonalization).

no substantial difference in the final results obtained from either the old spin mixing strategy [22, 42, 43, 44] or the one described here is found. Yet, for the sake of consistency we apply the same way of spin-mixing as described here throughout the paper.

2. Transport through a single quantum dot revisited

In this section, we focus on the application of tDMRG and ECA to the study of the conductance of a single quantum dot. The interacting portion of the Hamiltonian (1) is:

$$H_{\text{int}} = U n_{\text{dot},\uparrow} n_{\text{dot},\downarrow} + V_g n_{\text{dot}}, \quad (14)$$

where the Coulomb repulsion U represents the charging energy, V_g is the gate potential, and $n_{\text{dot}} = n_{\text{dot},\uparrow} + n_{\text{dot},\downarrow}$ is the dot's charge. The model is particle-hole symmetric at $V_g = -U/2$.

As has been shown in Ref. [19], tDMRG is capable of producing zero-temperature transport properties, such as the conductance as a function of gate potential or its dependence with a magnetic field. In that previous work, it was noticed that the behavior on finite systems with open boundary conditions was quite different depending on odd-even effects. When the total number of sites in both leads is even or odd, we have a $S_{\text{total}}^z = 1/2$ ground-state, while with an odd number of tight-binding sites in one lead and an even number in the other, the system has an overall $S_{\text{total}}^z = 0$ ground state. Here we present a detailed scaling analysis of static properties that explains why the latter type of clusters is preferable, as suggested in Ref. [19].

Finally, we discuss finite-size effects in the context of ECA, which are of similar origin, and we provide a quantitative comparison with exact results obtained through the Friedel sum rule [47] and DMRG.

2.1. Motivation: tDMRG results

Let us motivate our study by discussing results from tDMRG for the current through a quantum dot at small external biases. On an open chain with one embedded dot, we analyze three configurations: (i) an odd number of sites in both leads (*o1o*); (ii) an even number of sites in both leads (*e1e*), (iii) or an overall even number of sites (*o1e*). We repeated some of the main results obtained in Ref. [19] for the *o1e* cluster-type, which has mostly been used in that work. First, both at zero and finite U , the current exhibits a steady state in time, allowing us to assign a conductance value $G(N) = J(\tau)/\Delta V$ to each chain of finite length. Note that the length in time of such constant current is limited by twice the time that it takes the current to be reflected at the open boundaries. Second, performing a finite-size scaling of $G(N)$, one finds that it extrapolates, following a simple scaling law of the form $G(N) \sim 1/N$, to the known exact results for $U/t^2 \lesssim 13$. Typically, system sizes as large as $N = 300$ sites can be treated. Third, *e1e* clusters have been found to exhibit a slower convergence and generally, lower current values. Our discussion in this section will mostly focus on clusters with a total $S_{\text{total}}^z = 1/2$.

The behavior of a current driven by a small bias is illustrated in Fig. 2 for clusters of an intermediate length and at half filling: *e1e* clusters result in the smallest current, *o1e* clusters yield a larger current and exhibit the aforementioned steady state ($J(\tau) \approx \text{const}$), while *o1o* clusters allow for a substantially larger current that even exceeds - if considering the conductance $G = J/\Delta V$ - perfect conductance $G_0 = 2$. These differences are quite striking, considering that the system sizes used in Fig. 2 differ by only one site in the leads. It is also worth pointing out that these strong finite-size effects are in principle not caused by the presence of the dot, but can even be seen in the noninteracting case $U = 0$, as displayed in the inset of Fig. 2. Note that when the system size is increased, $J(\tau)/\Delta V$ measured on *o1o* clusters approaches perfect conductance from above.

The crucial difference between *o1e* on the one hand and the other two clusters on the other hand is the finite magnetic moment $S_{\text{total}}^z = 1/2$ present in the system in the case of an overall odd number of sites.

As we shall see, this finite moment is not homogeneously distributed over the system. Let us first explain the suppressed conductance seen in the case of the *e1e* clusters. Figure 3(a) shows the local spin density $\langle S_i^z \rangle$ vs. site for $N = 17$ sites and several values of $U/t = 0, 1, 2, 4$. Clearly, for any U , most of the S_{total}^z is carried by the central site, i.e., the quantum dot. The reason for this inhomogeneous distribution is easy to understand, considering the critical tendency of 1D systems towards antiferromagnetic (AFM) correlations at half filling. For that reason, the spin cannot be homogeneously distributed over all sites. We further observe that on open systems, the spins on the first and last tight-binding site point up, which then, with an even number of sites to the left and right of the dot, favors the spin on the dot to point up as well. In other words, both leads form an approximate singlet, leaving the remaining moment S_{total}^z on the dot. This is strictly true in the limit of $t' = 0$, where

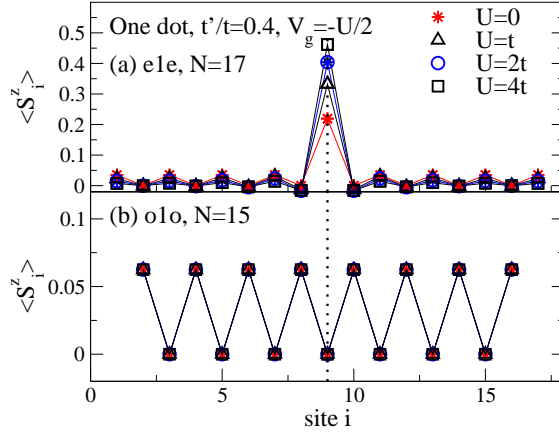


Figure 3. One dot, $t'/t = 0.4$, $V_g = -U/2$. Spin density $\langle S_i^z \rangle$, for (a) $N = 17$ sites ($e1e$) and (b) $N = 15$ sites ($o1o$) with $U/t = 0, 1, 2, 4$. (a): Even at $U = 0$, the z -component of the total spin is essentially carried by the central site, i.e., the dot. (b): Overall, a Néel-type pattern emerges, with equal positive $\langle S_i^z \rangle$ on each second site. The dotted vertical lines denote the position of the dot.

$\langle S_{\text{dot}}^z \rangle = 1/2$, while each lead has a vanishing $\langle S_{\text{total}}^z \rangle$. Increasing t' then reduces $\langle S_{\text{dot}}^z \rangle$. Upon increasing U at a fixed $t' > 0$, a larger fraction of S_{total}^z is pinned at the dot site, as charge fluctuations that tend to reduce the local moment are suppressed by increasing U .

Qualitatively, the situation of an $e1e$ cluster is equivalent to a quantum dot in the presence of a magnetic field: locally, the Z_2 symmetry $S_{\text{dot}}^z \leftrightarrow -S_{\text{dot}}^z$ is broken on $e1e$ clusters. A magnetic field is well known to split the Kondo resonance thus leading to a reduced conductance [47]. In order to support this picture, we use $e1e$ clusters and apply a magnetic field onto the dot:

$$H_{\text{field}} = h_{\text{dot}} S_{\text{dot}}^z; \quad S_{\text{dot}}^z = \frac{1}{2}(n_{\text{dot},\uparrow} - n_{\text{dot},\downarrow}). \quad (15)$$

As expected, when $\langle S_{\text{dot}}^z \rangle$ decreases upon applying the field h_{dot} , the current increases, as we show in Fig. 4. For the parameters of Fig. 4 ($N = 65$, $e1e$) it can be shown from the figure's inset that the spin projection on the dot vanishes at about $h_{\text{dot}} \approx 0.17$. Consistently, the current measured in tDMRG simulations is the largest for $h_{\text{dot}} \approx 0.25$ and reaches values similar as those observed using $o1o$ clusters of comparable system size. This clearly establishes a connection between the dots polarization and the achievable currents. Note further that $e1e$ clusters behave exactly like $o1o$ ones if the filling is kept at $(N \pm 1)/N$.

Finally, note that the finite spin projection in the cluster's ground-state (and thus the Coulomb-blockade behavior) is an issue of parameters. Increasing the coupling to the leads, i.e, t' , at fixed U and system size (say, $N = 33$, $e1e$) delocalizes the spin and a larger current is then measured in tDMRG calculations.

For the second type of clusters with a nonzero S_{total}^z , $o1o$, we find that the spin is equally distributed over every second site. This is displayed in Fig. 3(b). Since the out-most sites carry a positive $\langle S_i^z \rangle > 0$, the dot now has a nearly vanishing $\langle S_{\text{dot}}^z \rangle$.

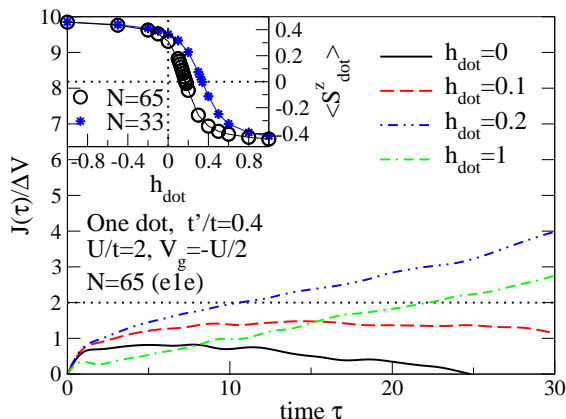


Figure 4. One dot, $t'/t = 0.4$, $U/t = 2$, $V_g = -U/2$. Main panel: Current $J(\tau)/\Delta V$ vs. time for $N = 65$ and several values for a magnetic field h_{dot} applied to the dot: $h_{\text{dot}} = 0, 0.1, 0.2, 1$ [see Eq.(15)]. The inset shows $\langle S_{\text{dot}}^z \rangle$ as a function of h_{dot} for $N = 33$ and 65 .

Consistent with the notion of $\langle S_{\text{dot}}^z \rangle \approx 0$, the spin projections on the dot and all other sites are practically independent of the Coulomb repulsion U , supporting the conclusion that the different behavior of these clusters is mainly of geometrical origin.

It is important to stress that at fixed odd N , both types of behavior can be produced: when shifting the dot in a $N = 33$ cluster by one site, a *17-dot-15* configuration is obtained. The current now behaves almost exactly like the one measured on an $N = 31$ (*o1o*, 15-dot-15) cluster and so does the z -component of the spin. The same holds for an asymmetric $N = 31$ cluster with a *16-dot-14* configuration: the dot now carries most of the S_{total}^z and the current is suppressed, similar to the case of $N = 33$ (16-dot-16, *e1e*). The corresponding DMRG results are not shown in the figures, but are quantitatively similar to Figs. 2 and 3. These considerations show that indeed the distribution of S_{total}^z , which depends on the geometry and model parameters, affects the conductance.

2.2. Static properties: Gate potential dependence

To render the line of reasoning outlined in the previous Sec. 2.1 more quantitative we proceed with a systematic discussion of static properties that are crucial to characterize a dot in the Kondo regime: spin and charge fluctuations on the dot, as well as spin-spin correlations between the dot and the leads. For this purpose, we focus on the parameter set $t'/t = 0.4$ and $U/t = 4$ and the dependence on the gate potential, keeping the full system at half filling.

First of all, let us recall some of the hallmark features of the single-impurity Anderson model at $T = 0$: (i) a slowly varying charge $n_{\text{dot}} \approx 1$ on the dot in a broad gate-potential window $-1 \lesssim V_g/U \lesssim 0$. This behavior is due to the Coulomb repulsion that does not permit a second electron to enter into the dot when there is already one. This property, i.e., the almost constant charge, becomes more pronounced

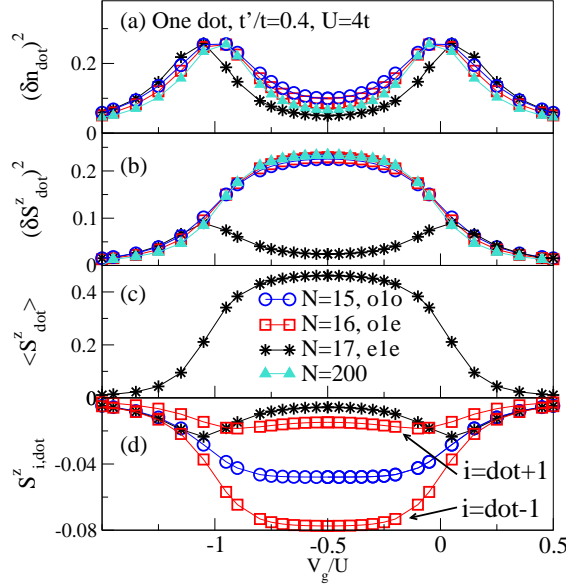


Figure 5. One dot, static properties computed with DMRG as a function of gate potential V_g/U at $t'/t = 0.4$, $U/t = 4$, comparing different cluster types: *o1o* ($N = 15$, circles), *o1e* ($N = 16$, squares), and *e1e* ($N = 17$, stars). Triangles are for a large system of $N = 200$ sites ($m = 300$ DMRG states). (a) Charge fluctuations $(\delta n_{\text{dot}})^2$; (b) spin fluctuations $(\delta S_{\text{dot}}^z)^2$; (c) local spin density $\langle S_{\text{dot}}^z \rangle$ on the dot; and (d) spin-spin correlations $S_{i,\text{dot}}^z$ between the dot and the first neighboring site in the leads. For *o1e* clusters such as $N = 16$, there is an asymmetry between the left and the right lead: the dot is mostly screened by the right lead, i.e., the one that has an odd number of sites.

as U/Γ increases, where Γ denotes the hybridization parameter. (ii) Enhanced spin fluctuations on the dot. (iii) Large charge fluctuations at the charge degeneracy points $V_g/U = -1, 0$, but a suppression of charge fluctuations in between. While the spin fluctuations at the particle-hole symmetric point increase with increasing U/Γ , the charge fluctuations decrease at the same time. Still, the conductance is always perfect, since the scattering of conduction electrons screens the magnetic moment, giving rise to the large spin fluctuations. Note that we characterize charge and spin fluctuations via:

$$(\delta S_{\text{dot}}^z)^2 = \langle (S_{\text{dot}}^z)^2 \rangle - \langle S_{\text{dot}}^z \rangle^2; \quad (\delta n_i)^2 = \langle n_i^2 \rangle - \langle n_i \rangle^2. \quad (16)$$

Properties (ii) and (iii) of the single-impurity Anderson model can nicely be seen in Figs. 5(a) and (b): *o1o* and *o1e* clusters exhibit a broad maximum in the spin fluctuations around the particle-hole symmetric point $V_g = -U/2$ [Fig. 5(a)], while charge fluctuations are suppressed. The maxima in $(\delta n_{\text{dot}})^2$ vs. V_g/U at $V_g/U = -1, 0$ are due to the charge degeneracy between states with $n_{\text{dot}} = 0$ and 1 and $n_{\text{dot}} = 1$ and 2 , respectively. For comparison, DMRG for $N = 200$ sites (triangles) are included in Fig. 5.

As for the *e1e* clusters, we emphasize that the main consequence of the finite spin projection $\langle S_{\text{dot}}^z \rangle$ present for $-1 \lesssim V_g/U \lesssim 0$ [see in Fig. 5(c)] on the dot is a reduction of spin fluctuations. A Kondo-resonance, however, which is at the heart of perfect

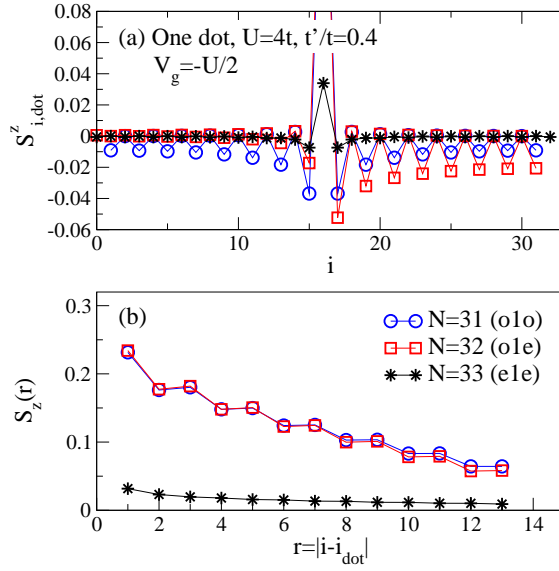


Figure 6. One dot, $t'/t = 0.4$, $U/t = 4$, $V_g = -U/2$. (a) Spin-spin correlations vs. site, (b) integrated spin-spin correlations $S_z(r)$ [see Eq. (18)] vs. distance r . Data are shown for $N = 31$ (circles, $o1o$), $N = 32$ (squares, $o1e$), $N = 33$ (stars, $e1e$).

transmission through a quantum dot at the particle-hole symmetric point, emerges as a consequence of virtual charge fluctuations due to scattering of conduction electrons off the impurity that cause substantial spin fluctuations on the dot, thus screening its moment [47].

Apart from spin fluctuations, and equally importantly, spin-spin correlations between the dot and the leads are affected as well. Figure 5(d) shows the spin-spin correlations between the dot and the first site in the leads:

$$S_{ij}^z = \langle S_i^z S_j^z \rangle - \langle S_i^z \rangle \langle S_j^z \rangle, \quad (17)$$

which are substantially smaller around the particle-hole symmetric point $V_g = -U/2$ on $e1e$ clusters than for other clusters. These two features illustrate the failure of $e1e$ clusters to harbor precursors of Kondo physics and to screen the impurity moment as long as system sizes are small. We shall discuss the finite-size scaling below.

Figure 2 suggests that, within tDMRG simulations, the largest current is seen on $o1o$ clusters. However, static properties, as displayed in Fig. 5, do not reflect this fact: both spin and charge fluctuations only slightly exceed those of other cluster types on small systems. Note that in the LDOS (not shown), the spectral weight at the Fermi level is systematically larger for this type of clusters than for others, corroborating the notion of an increased conductance, but not to an extent that would explain the large differences between $o1e$ and $o1o$ results shown in Fig. 2. The origin of the large current, therefore, remains still unclear, and requires a better understanding of the transient behavior of the current. Quantitatively consistent with the differences in currents measured on different clusters, we do observe a larger *local* gradient in the particle density defined as $\Delta n = n_{i_0+1} - n_{i_0-1}$, where i_0 labels the position of the quantum dot. One possible

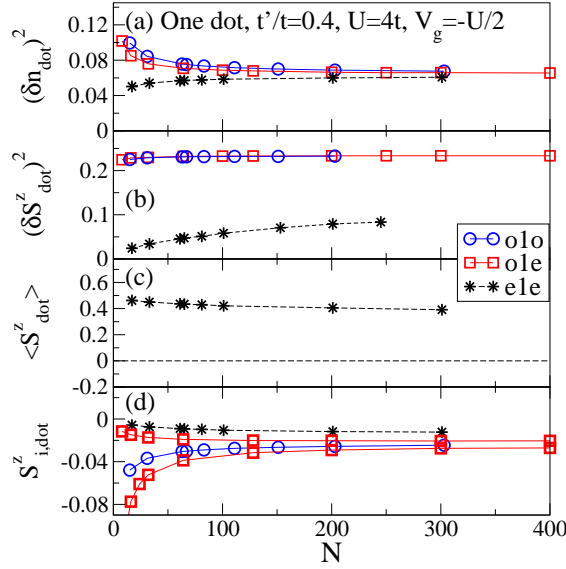


Figure 7. One dot, $t'/t = 0.4$, $U/t = 4$, $V_g = -U/2$. Finite-size scaling analysis of static properties: (a) charge fluctuations on the dot; (b) spin fluctuations on the dot; (c) local spin $\langle S_{\text{dot}}^z \rangle$ on the dot; (d) spin-spin correlations between the dot and its neighboring sites. Results are shown for $o1o$ (circles), $o1e$ (squares), and $e1e$ clusters (stars).

explanation may involve the modification of the leads due to the Néel pattern seen on $o1o$ clusters (see Fig. 3). Detailed investigations are under way to clarify this point and will be presented elsewhere.

Let us next discuss how the emergence of screening is reflected in the spatial extension of spin-spin correlations. DMRG results for spin-spin correlations [see Eq. (17)], measured away from the dot, and for their integral $S_z(r)$,

$$S_z(r) = \sum_{\substack{i \text{ with} \\ r'(i) \leq r}} S_{i, i_{\text{dot}}}^z; \quad r(i) = |i - i_{\text{dot}}|, \quad (18)$$

are displayed in Fig. 6(a) and (b), respectively, for $N = 31$ ($o1o$), $N = 32$ ($o1e$), and $N = 33$ ($e1e$). We first observe from Fig. 6(a) that, while the leads are symmetrically polarized in the case of $N = 31$, $o1e$ clusters mainly polarize one lead, namely the one that has an odd number of tight-binding sites. In this case, an *approximate* singlet is formed with this lead. When integrated over distance, the spin correlations behave quite similarly for these two cluster types, i.e., $o1e$ and $o1o$. Consistent with the notion of the absence of Kondo physics on small $e1e$ clusters, only small spin-spin correlations spread out into the leads for these clusters.

2.3. Static properties: Finite-size scaling

We proceed by discussing the finite-size scaling of static properties. Our DMRG results for system sizes $15 \leq N \leq 400$ are displayed in Fig. 7. The main observations are: (i) spin and charge fluctuations converge the fastest on $o1e$ clusters; (ii) in the case

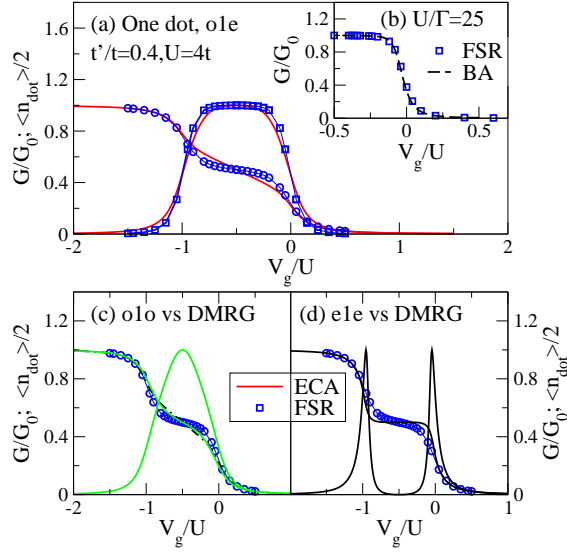


Figure 8. One dot, $t'/t = 0.4$, $U/t = 4$. (a) Conductance G and charge n_{dot} vs. gate potential V_g/U for $o1e$ (ECA, $N_{\text{ED}} = 12$, solid lines), and DMRG results for the charge and G obtained through the FSR (circles and squares, respectively). ECA results for an $1o$ cluster with $N_{\text{ED}} = 10$ sites are indistinguishable from the $o1e$ curve. (b): Comparison of conductance obtained from the Friedel sum rule using DMRG data for the charge n_{dot} ($N = 300$, $m = 500$, $U/t = 0.5$, $t'/t = 0.1$) with Bethe-ansatz results from Ref. [48]. (c) Conductance G and charge n_{dot} vs. gate potential V_g/U for $o1o$ (ECA, $N_{\text{ED}} = 11$, solid lines), and DMRG results for the charge (circles). (d) Conductance G and charge n_{dot} vs. gate potential V_g/U for $e1e$ (ECA, $N_{\text{ED}} = 9$, solid lines), and DMRG results for the charge (circles).

of $e1e$, the dot carries a large, finite $\langle S_{\text{dot}}^z \rangle$ that decays slowly with N , suppressing spin fluctuations and spin-spin correlations with the dot's neighboring sites; (iii) antiferromagnetic spin-spin correlations $S_{i,\text{dot}}^z$ are enhanced in the case of $o1o$ clusters on small systems, while on $o1e$ clusters, mainly the lead with an odd number of sites develops AFM correlations.

2.4. ECA results for the conductance

Early studies [24] using this technique have phenomenologically proposed that for one dot, the best results are obtained when it is neighbored by an odd number of sites ($o1o$), while $e1e$ clusters exhibit Coulomb-blockade behavior. Using insights of Sec. 2.2 and 2.3, we can now explain this observation on a more rigorous basis. Small $e1e$ clusters typically locate the $S_{\text{total}}^z = 1/2$ to a large extent onto the quantum dot, thus giving rise to a Zeeman-split resonance. Consistently, we find a charge gap in the local density of states (LDOS). While the embedding procedure manages to redistribute spectral weight in the LDOS quite well [26] it does not close the charge gaps given by the exactly solved interacting region.

For illustration, we show ECA results for one dot at $t'/t = 0.4$, $U/t = 4$ and all three cluster types in Fig. 8(a), (c), and (d). The figure also contains the conductance

as obtained from the Friedel sum rule (FSR) using the charge computed with static DMRG [47]:

$$G = G_0 \sin^2(\pi n_{\text{dot}}/2), \quad (19)$$

where $G_0 = 2$ due to spin degeneracy. Here we claim that the charge n_{dot} can be obtained to high precision from static DMRG. To support this we show a comparison for the conductance derived from Eq. (19) with exact Bethe-ansatz results [48] in Fig. 8(b) for $U/\Gamma = 25$. Note that in the wide-band limit $U < 4t$, the hybridization parameter is $\Gamma = 2\pi t'^2 \rho_{\text{lead}}$, and since we work with semi-infinite-leads, $\rho_{\text{lead}} = 1/(\pi t)$ [39] Our DMRG results are for $U = 0.5t$, $t'/t = 0.1$ and we find excellent agreement with the results of Ref. [48].

Clearly, the $o1e$ clusters are closest to the FSR. In Fig. 8(d), we further observe a Coulomb blockade type-of behavior for $e1e$ clusters. Regarding the $o1o$ cluster, although it qualitatively provides the correct physical description, the conductance plateau comes out too narrow as the charge around the particle-hole symmetric point $V_g = -U/2$ varies too fast as compared to the DMRG result [see Fig. 8(c)]. Note that the ECA results for the charge n_{dot} as displayed in Fig. 8 are obtained *after* embedding by integrating over the imaginary part of the dot's onsite Green's function [26].

A further improvement of results can be achieved by using a transformation onto bonding and anti-bonding orbitals in the Hamiltonian for one dot, Eqs. (1), (14):

$$b_{i,\sigma}^\dagger = \frac{1}{\sqrt{2}}[c_{i_L,\sigma}^\dagger + c_{i_R,\sigma}^\dagger]; \quad a_{i,\sigma}^\dagger = \frac{1}{\sqrt{2}}[c_{i_L,\sigma}^\dagger - c_{i_R,\sigma}^\dagger]. \quad (20)$$

Here, the index i measures the distance away from the dot and i_L, i_R are the corresponding indices in the two semi-infinite leads. The transformation decouples the dot from the anti-bonding states, leaving it coupled only to the bonding states. This is technically a great simplification as systems almost twice as large can now be treated. While such transformation cannot be used for the spatially asymmetric $o1e$ clusters, it works for $e1e$ and $o1o$. We observe that exactly the same result is found for $e1e$, comparing, say, the full $N = 9 = 4\text{-dot-}4$ with the symmetrized $\text{dot-}4$ clusters. Here, the spin still cannot be screened in a singlet state. For $o1o$, the results substantially improve, as now, effectively a $\text{dot-odd} (1o)$ cluster is solved that has an overall $S_{\text{total}}^z = 0$ ground-state, allowing for singlet formation. This gives results similar to those obtained from an $o1e$ configuration with less computational effort, as a smaller cluster is diagonalized. Slightly better results may even be obtained from increasing the size of the cluster. This further supports the idea that it is the $o1$ part of the $o1e$ configuration that is relevant for describing the many-body effects at the Fermi level of the system.

Our observations lend strong support to the idea that when the global quantum numbers of the exactly solved cluster allow for a singlet state to be the ground state – as is the case for $o1e$ and $1o$ clusters – then a precursor of the Kondo effect can be seen even on small ED clusters, with a favorably fast convergence with system size.

Finally, Fig. 8(a), (c), and (d) suggest a way to gauge the quality of ECA data even in a situation where no exact results for the conductance are available. We see that

the cluster type that produces the best charge vs gate potential curve yields the best G vs. V_g curve as well. Thus, the use of an *independent* technique, such as DMRG, that allows to reliably compute static properties such as charges or fluctuations is well suited to identify the *optimum* cluster type.

2.5. One quantum dot: Summary

Let us summarize our observations from this Sec. 2. We can understand the behavior of reflection-symmetric clusters with an odd number of sites with a finite S_{total}^z in terms of rigid spins $\langle S_i^z \rangle$ pinned to certain sites. In the case of $e1e$, the dot is mostly polarized and carries a finite magnetization. This is qualitatively equivalent to the application of a magnetic field that causes Zeeman splitting of the Kondo resonance and, thus, a suppression of the conductance [47]. For the case of $o1o$ clusters, the magnetic moment is mainly distributed over the leads. Due to the antiferromagnetic correlations, a Néel-type order emerges. For comparable system sizes, a substantially larger current is observed on these clusters, which however, does not exhibit a steady state in tDMRG simulations – i.e., a current that is constant in time – for $t' \neq t$. The origin of this observation is the subject of ongoing investigations.

Our analysis further suggests that either $o1e$ or $1o$ clusters are best suited to study the emergence of Kondo physics with techniques such as tDMRG or ECA, while on system sizes accessible to these techniques, $e1e$ clusters yield qualitatively different results with essentially a Coulomb blockade type of behavior. The overall conclusion is that in order to provide a reliable description of the many-body effects at the Fermi level, clusters with a $S_{\text{total}}^z = 0$ ground state are necessary. Among these, the advantage of $1o$ clusters is that larger system sizes can be accessed.

3. Three Dots

We now turn to a more complicated case, three serially coupled dots, as shown in Fig. 1(b). Apart from the interest in the emergence of Kondo physics, many quantum dots arranged in an array can be considered an interpolation between a single localized impurity and a bulk Mott insulator. In the first case, the transmission at half filling is perfect, but zero in the later due to the presence of the Mott gap.

The interacting region is described by

$$H_{\text{int}} = -t'' \sum_{i=1}^2 (c_{i,\sigma}^\dagger c_{i+1,\sigma} + \text{H.c.}) + U \sum_{i=1}^3 n_{i,\uparrow} n_{i,\downarrow} + \sum_{i=1}^3 V_g n_i. \quad (21)$$

To simplify the notation, we will refer to the dots as **D1**, **D2**, and **D3**, where **D2** is the central dot. We focus on the behavior at the particle-hole symmetric point unless stated otherwise. In the case of three dots, we distinguish between odd-3-odd ($o3o$), odd-3-even ($o3e$), and even-3 even ($e3e$) clusters.

Following Ref. [34, 35], for large $t'' \geq U$, the three dots can be viewed as a molecule with, at half filling, two electrons occupying its lowest state, and a resulting $S_{\text{total}}^z = 1/2$

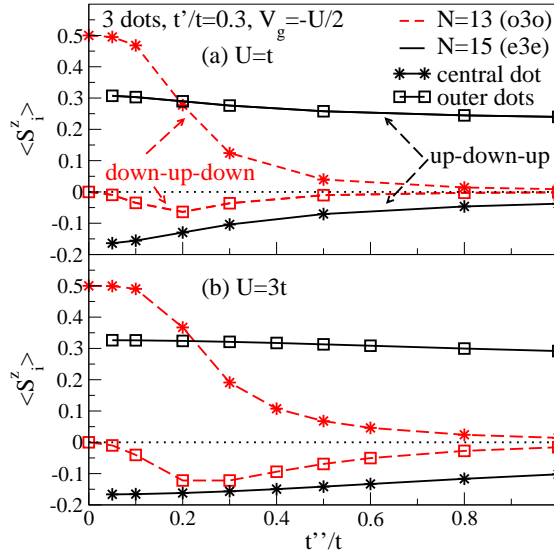


Figure 9. Three dots, $t'/t = 0.3$, $U/t = 1$ (a) and $U/t = 3$ (b). (a) Spin projection $\langle S_i^z \rangle$ vs. t''/t for the outer dots (squares) and the central dot (stars) for $N = 13$ ($o3o$, dashed lines) and $N = 15$ ($e3e$, solid lines) clusters. On $o3e$ clusters, $\langle S_1^z \rangle \approx 0$ within the error bounds of DMRG measurements. (b) Same as in (a), but for $U/t = 3$. Note that the magnitude of the fixed spins for both clusters ($o3o$ and $e3e$) increase with the value of U .

from the third electron. For intermediate $t'' \sim 0.3U$, it has been suggested that the three dots behave as a linear antiferromagnet due to strong AFM spin-spin correlations between them. Finally, at small $t'' \ll U$, the system enters a very subtle two-stage Kondo regime. First, and below a Kondo scale $T_K^{(1)}$, the outer dots form a Kondo singlet with their adjacent leads. Then, at temperatures below a second Kondo scale $T < T_K^{(2)} < T_K^{(1)}$, the central dot is screened by the quasi-particles of the two Fermi liquids formed by the outer dots and their leads. Although $T_K^{(2)}$ is orders of magnitude smaller than $T_K^{(1)}$ [49, 34] which renders an experimental confirmation of the effect a challenging task, nevertheless the two-stage process conceptually plays an important role for extremely low temperature physics. In all three cases and at temperature $T = 0$, the system possesses a spin $S = 1/2$ Kondo ground state. In relation with the AFM regime, we wish to point out that in all regimes, AFM spin-spin correlations exist. It remains unclear to us whether the so-called AFM regime has specific transport properties or not, while the molecular and the two-stage Kondo regime are clearly distinguishable by the conductance's temperature dependence.

Concerning the issue of the conductance, several studies using a variety of approaches such as perturbation theory [32], NRG [36, 35], and functional renormalization group [21] report perfect conductance at the particle-hole symmetric point due to the Kondo effect. An earlier ECA work on this model [25] is at odds with this conclusion. In particular, an exact zero of the conductance at the particle-hole symmetric point has been found for all values of $t'' \lesssim 0.5t$.

We show that the vanishing of G at $V_g = -U/2$ at $t''/t \lesssim 0.3$ is due to the choice

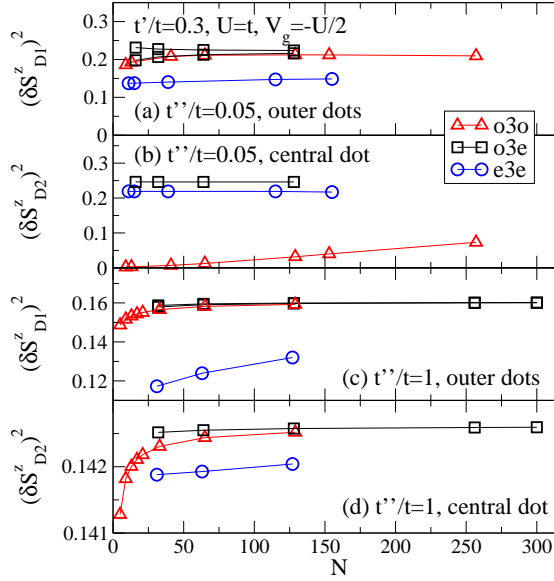


Figure 10. Three dots, $t'/t = 0.3$, $U/t = 1$. Finite-size scaling of spin-fluctuations on the dots for $t''/t = 0.05$ [(a),(b)] and $t''/t = 1$ [(c),(d)]. DMRG results are depicted for all three cluster types: $o3e$ (squares), $e3e$ (circles), and $o3o$ (triangles).

of $o3o$ clusters for the ECA calculations of Ref. [25]. At large $t'' > t'$, this dip is an artefact of certain approximations taken in the embedding procedure: if we perform the ECA according to the prescription of Sec. 1.2 without mixing Green functions for spin up and down before the embedding is carried out, this artifact disappears.

We shall outline below that the optimum cluster type – in the sense of fastest convergence of static properties with system size – is $o3e$. On this cluster type, no spurious dip at $V_g = -U/2$ exists, independent of the spin-mixing strategy adopted in ECA calculations.

The section is organized as follows: We first analyze static properties and their finite-size scaling in Sec. 3.1. Section 3.2 contains our ECA results, obtained following the procedure discussed in Sec. 1.2, for the conductance. In Secs. 3.3 and 3.4, we briefly discuss the problem one encounters in the regime of $t'' \lesssim t'$ using $o3e$ and $o3o$ clusters, respectively.

3.1. Static properties: Finite-size scaling

Let us first consider the three dots isolated from the leads ($t' = 0$) at $U = t$ as a function of t''/t , which will help to understand $e3e$ and $o3o$ clusters. In the $S_{\text{total}}^z = 1/2$ subspace, the two lowest-lying states are both doublets ($S = 1/2$), however, with different spin projections $\langle S_i^z \rangle$ on the dots. The ground state has – schematically – an up-down-up pattern, while the first excited state realizes an up-up-up structure, with most of the $S_{\text{total}}^z = 1/2$ on the central dot. The actual distribution of $\langle S_i^z \rangle$ depends on t''/U for a given t' , but when the isolated cluster is embedded in leads with an overall odd number of sites (i.e., all sites in the leads plus the three dots), the two low-lying states are mixed

with different weights: on $o\beta o$ clusters, a down-up-down configuration is preferred, while on $e\beta e$ ones, the original ground-state pattern (up-down-up) prevails. This, again is a consequence of the open boundary conditions and the tendency of one-dimensional systems towards antiferromagnetic correlations at half filling, as discussed in Sec. 2. We illustrate this in Fig. 9 where we plot $\langle S_i^z \rangle$ vs. t''/t' for $N = 13$ ($o\beta o$) and $N = 15$ ($e1e$). We further see that, as a function of increasing t''/t , the spin projection on the central dot is substantially reduced and moved to the leads in the case of $o\beta o$. The large $\langle S_i^z \rangle$ located on the outer dots seen in the case of $e\beta e$ decays much slower as a function of t''/t .

The rigid spins on either of these cluster types imply suppressed spin fluctuations for the individual dot (**D2** in the case of $o\beta o$ and **D1**, **D3** in the case of $e\beta e$) as well as modified spin-spin correlations. As two case examples, we present the finite-size scaling of such quantities with system size in Figs. 10 and 11 for $U = t$, $t'/t = 0.3$ with $t''/t = 0.05$ and $t''/t = 1$, respectively.

Let us first discuss $e\beta e$ clusters (circles in Figs. 10 and 11). Due to the large spin projection on the outer two dots, spin fluctuations as well as the spin-spin correlations with the first site in the leads are suppressed. The latter is an indicator of how strongly the dots polarize the leads. Since the spin-projections $S_{\mathbf{D1}}^z$ and $S_{\mathbf{D3}}^z$ are – both at small and large t'' – only slowly redistributed to other sites as the system size grows, as is evident from Figs. 10(a) and (c), we conclude that these clusters will produce low conductance values or currents in ECA and tDMRG calculations, respectively.

The $o\beta o$ clusters (triangles in Figs. 10 and 11) are the ones originally used in Ref. [25]. Figure 10(b) reveals that spin fluctuations on the central dot are suppressed in the limit of small $t'' \lesssim t$, which is due to a large fraction of S_{total}^z located on the central dot. This cluster type is therefore geometrically similar to the $e1e$ clusters of one quantum dot. As it is illustrated for the case of $t''/t = 0.05$ in Fig. 10(b), the spin fluctuations on the central dot increase very slowly with system size. We may therefore argue that here the central dot fails to participate in a Kondo effect, especially in the two-stage Kondo regime. We further believe that this pathology, i.e., the finite $S_{\mathbf{D2}}^z$, is at the origin of the conductance dip at $V_g = -U/2$ observed with ECA in Ref. [25], similar to the case of one quantum dot. We will further elaborate on this analogy in Sec. 3.4.

Clusters with an overall $S_{\text{total}}^z = 0$ (i.e., $o\beta e$ – squares in Figs. 10 and 11) exhibit the least significant finite-size effects and local fluctuations converge the fastest with system size N , while spin-spin correlations exhibit an asymmetry between the left and right lead. As a conclusion, we may expect the most reliable results for conductances from this cluster type, and this notion will further be corroborated by ECA results in Sec. 3.2.

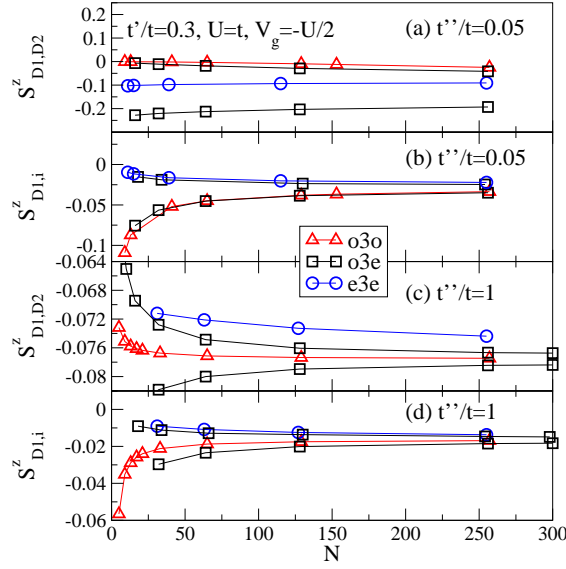


Figure 11. Three dots, $t'/t = 0.3$, $U/t = 1$. Finite-size scaling of spin-spin correlations for $t''/t = 0.05$ [(a),(b)] and $t''/t = 1$ [(c),(d)] (DMRG). (a) and (c): spin-spin correlations between the central dot and the outer ones. (b) and (d): spin-spin correlations between the outer dots and the first site in the adjacent lead.

3.2. ECA results for the conductance of three dots: Comparison of cluster types

3.2.1. Gate-potential dependence In this section, we present ECA results for the conductance G and n_{total} for the three dots configuration as a function of the gate potential, comparing all three cluster types. The ECA results (solid lines) are depicted in Fig. 12(a) ($o3e$), (b) ($o3o$), and (c) ($e3e$). As expected from the discussion of static properties in Sec. 3.1, the n_{total} results for $o3e$ clusters obtained after embedding agrees very well with DMRG results [squares, see Fig. 12(a)], while the results from other clusters systematically deviate from DMRG data [squares, see Figs. 12(b) and (c)]. Note the steeper slope of n_{total} around the particle-hole symmetric point seen on $o3o$ clusters, which gives rise to a narrower peak in the conductance. In Fig. 12(c) [solid lines], it is shown that $e3e$ clusters produce the expected Coulomb-blockade behavior due to the rigid spins on the outer dots (see Fig. 9).

Since the system of three dots coupled to leads is a Fermi-liquid [32, 35, 49], one expects a Friedel sum rule to be valid here, e.g., of the form

$$G = G_0 \sin^2(\pi\mathcal{N}/2). \quad (22)$$

Unfortunately, there is no agreement as to what needs to be inserted for \mathcal{N} in this case: using n_{total} results in an exactly vanishing conductance whenever n_{total} is even – a result that is known to be incorrect for the case of two quantum dots [23, 50, 51, 52]. Early work suggests \mathcal{N} to be the *difference* between states with even and odd parity, i.e., the independent scattering channels, – a result that to the authors' best knowledge has so far only been proven to be true for the noninteracting case [53]. With either ansatz for \mathcal{N} in Eq. (22), the three Kondo-peaks are found at odd total charge, i.e., $V_g/U = -1/2$

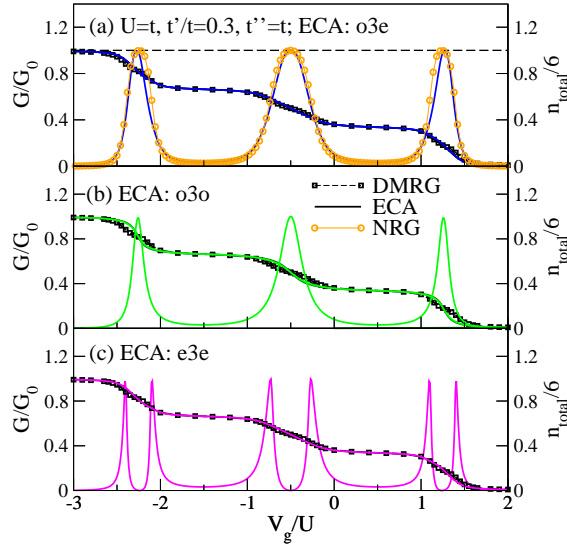


Figure 12. Three dots, $t'/t = 0.3$, $U/t = 1$, $t''/t = 1$. Conductance and charge vs. gate potential V_g/U . (a) ECA results for the conductance and charge for an $o3e$ cluster (solid lines, $N_{\text{ED}} = 12$) vs. DMRG results for the charge n_{total} (squares) and NRG results ([54], circles). ECA and DMRG results for the charge are indistinguishable on the scale of the plot. (b) ECA results for an $o3o$ cluster (solid lines, $N_{\text{ED}} = 9$). (c) ECA results for an $e3e$ cluster (solid lines, $N_{\text{ED}} = 11$). DMRG results for n_{total} (squares) are included in (b) and (c) for comparison.

and $V_g/U \approx -2.26, 1.26$, in very good agreement with our ECA data. Figure 12(a) also shows NRG data from Ref. [54]. The agreement between ECA and NRG [54] is quite good, especially for the central Kondo peak and the Coulomb blockade valleys at $n_{\text{total}} = 2, 4$. We mention that different ansatzes in Eq. (22) mainly result in differences in the conductance in the Coulomb Blockade valleys.

3.2.2. Behavior at the particle-hole symmetric point Thus far, we have seen that with $o3e$ clusters, we obtain the best agreement with NRG regarding the gate-potential dependence. Let us next address the value of the conductance at the particle-hole symmetric point as a function of t'' . This will indicate what parameter range can be accessed when decreasing t''/t using $o3e$ clusters.

Figure 13 compares $o3e$ and $o3o$ ECA conductance results at the particle-hole symmetric point for $U = t$ and $U = 3t$. In the former case, where $o3o$ clusters with $N_{\text{ED}} = 5, 9$ are compared with an $o3e$ cluster with $N_{\text{ED}} = 12$, it is shown that there is barely any difference between the results for the two different types of clusters: for $t''/t \approx 0.5$, the correct result $G/G_0 = 1$ is recovered. However, in the later case ($U = 3t$), there is a pronounced difference between $o3o$ ($N_{\text{ED}} = 9$) and $o3e$ ($N_{\text{ED}} = 10$) results: the vanishing of the conductance at the particle-hole symmetric point for the $o3o$ cluster occurs at a much higher value of t''/t than for the $o3e$ cluster. The reason for that can be understood by analyzing the results in Fig. 9, where the fixed net-spin present in $o3o$ clusters is compared for $U = t$ [panel (a)] and $U = 3t$ [panel (b)]. It is intuitively clear

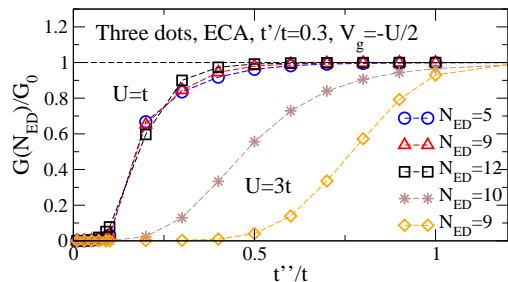


Figure 13. ECA results for three dots with $t'/t = 0.3$, $U/t = 1.0$, and $U/t = 3.0$: Variation of the conductance with t'' at the particle-hole symmetric point $V_g = -U/2$. The results for $U/t = 1.0$ are calculated using $o\beta o$ with $N = 5$ sites (circles) and $N = 9$ sites (triangles), as well as $o\beta e$ clusters with $N = 12$ sites (squares). At this value of U/t , there is barely no difference between the two types of clusters, i.e., as the value of t'' increases, the conductance at the particle-hole symmetric point changes from 0 to G_0 at basically the same value of t'' , independent of cluster type. However, the same is not true for the $U/t = 3.0$ results ($N = 10$ for $o\beta e$ cluster (stars) and $N = 9$ for $o\beta o$ cluster (diamonds)). It is clear that the $o\beta o$ clusters result vanish $G = G_0$ at substantially higher t'' than the $o\beta e$ ones. As explained in the text, this is caused by a larger fixed spin in $o\beta o$ clusters at higher U values.

that a larger value of U will, for a fixed t'' , increase the magnitude of the fixed spins in the three dots since charge fluctuations are more strongly suppressed (see Fig. 9). Therefore, as pointed out above, $o\beta e$ clusters, with $S_{\text{total}}^z = 0$, provide better results also at the particle-hole symmetric point when compared to $o\beta o$ clusters. In the next subsection, we will discuss why the conductance eventually also vanishes for low t'' values in the $o\beta e$ cluster, which do not exhibit finite values of $\langle S_i^z \rangle$.

We now turn to a finite-size scaling analysis of $G(N)$ at the particle-hole symmetric point. Using cluster sizes within ECA that are numerically tractable (i.e., $N_{\text{ED}} \lesssim 13$), we find that, at the particle-hole symmetric point, for $U/t = 1.0$, $G(N_{\text{ED}})/G_0$ scales to one with $1/N_{\text{ED}}$ for $t''/t \gtrsim 0.3$ (upper panel in Fig. 14). In addition, it is clear from the results shown in Fig. 14 (b) that, the larger the value of U , the higher is the value of t'' below which one cannot clearly ascertain the extrapolation to $G(N_{\text{ED}})/G_0 = 1$ at small t'' values. Obviously, this happens because the Kondo temperature of the second stage decreases with U , causing the ECA conductance to vanish at a larger t'' . Summarizing, both $o\beta o$ and $o\beta e$ clusters produce results in qualitative agreement with other techniques at $V_g = -U/2$ only above certain values of t'' . For $U/t = 1$, $G = G_0$ can be obtained by extrapolation with a $G(N_{\text{ED}}) = G_0 - \text{const}/N_{\text{ED}}$ function for $t''/t \gtrsim 0.2$. For smaller t'' , system sizes are too small to establish a clear trend towards $G(N_{\text{ED}})/G_0 = 1$ due to a finite level spacing.

We are led to conclude that ECA captures quite well the correct physics depending upon the parameters and the cluster taken. The optimum cluster can be identified by analyzing the finite-size scaling of, e.g., the charge, with independent techniques such as DMRG.

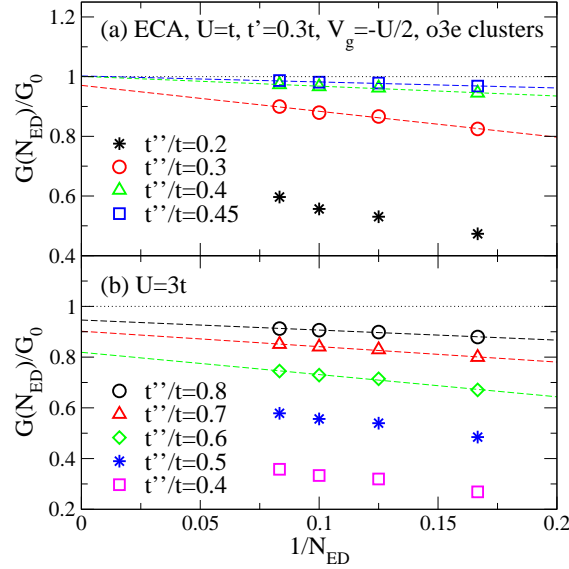


Figure 14. Three dots, $t'/t = 0.3$, $U/t = 1$ (a) and $U/t = 3$ (b). (a) Finite-size scaling analysis of ECA results on $o3e$ clusters for $G(N_{\text{ED}})$ at the particle-hole symmetric point ($V_g = -U/2$) for $t''/t = 0.45, 0.4, 0.3, 0.2$ (squares, triangles, circles, and stars). Dashed lines indicate $f(N_{\text{ED}}) = a + b/N_{\text{ED}}$ fits to $G(N_{\text{ED}})$. (b) Same as in (a), but now for $U/t = 3$, and $t''/t = 0.8, 0.7, 0.6, 0.5$, and 0.4 (circles, triangles, diamonds, stars, and squares). Note that in this case, the threshold, below which the convergence to G_0 cannot be ascertained, is higher than in the $U/t = 1$ case.

3.3. $o3e$ clusters in the small t'' regime

We next wish to illustrate the difficulties encountered in the small t'' regime, for $o3e$ clusters. Unfortunately, when t'' is decreased, the asymmetry between the two outer dots on $o3e$ becomes quite pronounced. Note that the total charge from ECA still agrees well with DMRG down to very small t'' (not shown). However, spin-spin correlations on small $o3e$ clusters suffer from (i) the aforementioned asymmetry between the two outer dots (see Fig. 11), and (ii) the fact that the central dot is basically decoupled from the leads (at the Fermi energy). This is indicated by small spin-spin correlations between the central dot and the first site in the leads, which indicates that the effective exchange with the leads is smaller than the energy level spacing. Consistent with the first point discussed here, in accordance to the LDOS calculated with ECA for an $o3e$ configuration, at small t'' and for $V_g = -U/2$ (particle-hole symmetric point), only one of the outer dots develops a sharp Kondo resonance, namely the one connected to the *odd* lead. The dot connected to the *even* lead can only be Kondo screened through the other two dots. However, at low values of t'' , this mechanism becomes ineffective and this dot presents very low LDOS at the Fermi energy, leading to the suppression of the conductance at the particle-hole symmetric point, as seen in Fig. 13. Therefore, even for the optimum cluster type $o3e$, the two-stage Kondo regime, for small values of t'' , seems to be out of reach within the real-space variant of this technique and current computational resources.

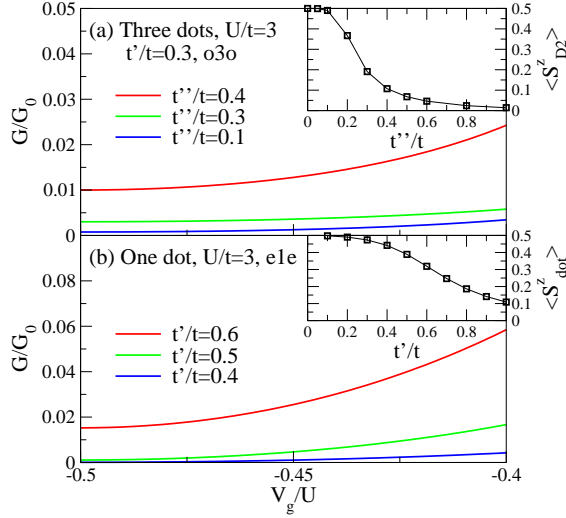


Figure 15. ECA results for the conductance as a function of gate potential. (a) Three dots geometry, several values of inter-dot hopping ($t''/t = 0.4, 0.3, 0.1$) and $U/t = 3$, $t'/t = 0.3$ and $o3o$ clusters. As t'' decreases, a suppression of the conductance at and around the particle-hole symmetric point occurs. The inset shows the accumulation of the net spin in the central dot with decreasing t'' . (b) *Single-dot* configuration: $U/t = 3.0$, and several $t'/t = 0.6, 0.5, 0.4$; using $e1e$ clusters. As discussed in Section 2, this kind of cluster, $e1e$, exhibits strong finite-size effects originating from the presence of a fixed spin at the quantum dot. The progressive accumulation of the fixed spin in the QD with decreasing t' is shown in the inset. The similarity between the results in panels (a) and (b) is obvious.

3.4. Comparison of ECA results for one dot ($e1e$) and three dots ($o3o$)

In this section, the authors wish to lend further support to the notion that the ECA results for the three dots obtained with an $o3o$ configuration originate in finite-size effects that can be linked to finite-size effects of the $e1e$ configuration for a single dot, as analyzed in Sec. 2.

To this end, we compare ECA results for three dots with ECA results for one dot, focusing on $e1e$ and $o3o$ cluster types. From DMRG calculations, we have seen that both $e1e$ and $o3o$ clusters localize most of the S^z_{total} on the central site, resulting in an effective Zeeman splitting of the Kondo resonance of the central quantum dot. For both clusters, charge gaps open that are systematically larger than those seen for other cluster types. As already mentioned above, previously published ECA results for three dots [25], which have not been confirmed by other techniques, report the vanishing of the conductance at the particle-hole symmetric point. This is due to a particularly slow convergence with cluster size of the energy spectra for both $e1e$ and $o3o$ configurations, as already illustrated in the previous sections by DMRG calculations. Notice that in the previously published ECA calculations [25] the choice of cluster type to be solved by Lanczos – $o3o$ – was guided by the intuition that the multi-quantum-dot complex should essentially behave as a ‘molecule’, i.e., the localized many-body state to be screened by the leads should behave qualitatively similar to a single quantum dot [24]

This has led to the common practice of using the ‘preferred’ single-dot configuration, i.e., $o1o$. While, even in the case of one dot, within the embedding technique [see the respective discussion in Sec. 2.4], this choice is optimum only after the transformation Eq. (20) has been exploited, the choice of $o\beta o$ for three dots is disadvantageous due to the aforementioned analogy to $e1e$ clusters. Also, no transformation of the type of Eq. (20) exists in the case of three dots that would decouple one channel. In the case of three dots, the two subsystems obtained after applying Eq. (20) are not decoupled due to residual many-body interactions between them.

We now emphasize the analogy between $e1e$ (for one dot) and $o\beta o$ (for three dots) in more detail. To understand the analogy between $e1e$ and $o\beta o$, one has to refer back to Fig. 9, where the distribution of the net spin (present in the $o\beta o$ cluster) between the three QDs is discussed. For $t'' \gg t'$, the QDs share very little of the net spin, which is in reality mostly distributed among the tight binding sites, illustrating the similarity of the $o\beta o$ cluster with the $o1o$ cluster in relation to avoiding any finite size effects associated to the presence of the net spin. This picture starts to change as t'' starts to decrease. Once $t'' \sim t'$, the net spin starts to localize evenly in the three QDs, before getting completely concentrated in the central dot for $t'' \ll t'$ (see Fig. 9). As long as the majority of the net spin finds itself in the central dot, one should expect that the conductance of the $o\beta o$ cluster will resemble that of an $e1e$ cluster [see Fig. 8(d)], at least around the particle-hole symmetric point. This point is made more evident in Fig. 15, which shows the conductance as a function of gate potential for three dots [panel (a)] and one dot [panel (b)]. It displays a comparison of the conductance variation with t' (for $e1e$) and t'' (for $o\beta o$, at fixed t') around the particle-hole symmetric point. As suggested by the discussion above, as t'' becomes a fraction of t' , and the net spin accumulates in the central dot, one should find similarities in the $o\beta o$ conductance with that for $e1e$. This point is made more clear by the results shown in the insets: in panel (a), the value of $\langle S_{\text{dot}}^z \rangle$ at the central dot is plotted for the same range of t'' values as for the conductance. Note the similarity with the inset in panel (b), where the equivalent results for $e1e$ are shown. It is this finite size effect of spin accumulation in the central dot that suppresses the conductance at (and around) the particle hole symmetric point for both $e1e$ and $o\beta o$.

It is worth noticing that a comparison of the LDOS for low values of t'' in $o\beta o$ with that in $e1e$ (not shown) supports the argument that the suppression of the conductance around the particle-hole symmetric point for $o\beta o$ originates from the same finite size effect present in $e1e$.

4. Summary

In this work, we have performed an extensive finite-size scaling analysis of fluctuations and correlations in nanostructures, such as one and three quantum dots embedded into leads of a finite length. Strong differences in the finite-size scaling behavior emerge depending on even-odd effects. These findings are relevant for the interpretation

of results from numerical approaches for the calculation of the conductance of nanostructures that are based on analyzing clusters of finite length with open boundary conditions, such as time-dependent DMRG or cluster-embedding approaches (ECA). To qualitatively capture precursors of the Kondo effect, clusters with a $S_{\text{total}}^z = 0$ are best suited, as electrons on the dot at half filling naturally participate in a singlet state. Other cluster types with an overall $S_{\text{total}}^z = 1/2$ may be *far* away from capturing Kondo physics in the sense of slow convergence with system size. For certain configurations, most of the $S_{\text{total}}^z = 1/2$ is found on the central site, which, if this site is a quantum dot, causes a gap in the local density of states at the Fermi level, reminiscent of the Zeeman-splitting of the conductance due to the application of a magnetic field.

These findings help to understand the puzzling discrepancy between ECA results for three dots and those of other techniques: the vanishing of the conductance at the particle-hole symmetric point obtained with ECA is only seen on certain cluster types, but disappears when the three dots are embedded in a cluster with an overall $S_{\text{total}}^z = 0$. Hence, the use of such clusters substantially extends the range of applicability of this technique. While parameter regimes with exponentially small energy scales such as two-stage Kondo regimes are difficult to be accessed with this technique in its real-space variant, very good agreement with exact results such as the Friedel sum rule in the case of one dot or NRG in the case of three dots is otherwise found in other regions of the parameter space.

Another model that exhibits a two-stage Kondo effect is two dots coupled in a T-shape geometry [49, 55]. At half filling, the conductance is found to vanish [49, 55] a picture that disagrees with the results of ECA calculations in the two-stage Kondo regime [25]. We have performed a similar analysis of static properties and ECA results on different cluster types for this geometry, with results not shown here. While in the regime of large t''/U , where t'' is the hopping between the two dots, good agreement between the Friedel sum rule [49] and ECA is found, the two-stage Kondo regime, which emerges at small t'' [49, 55] suffers from strong finite-size effects. Unfortunately, no cluster type shows a particularly fast scaling behavior here. A more detailed discussion will be presented elsewhere [26].

We further propose that a comparison of ECA results for static properties, such as the total charge of a nanostructure as a function of gate potential, against independent techniques, such as DMRG, is helpful to determine the optimum cluster type. Promising results from a new version of ECA that incorporates a discretization of the DOS of the leads clearly indicate that the range of validity of the embedding approach can further be improved [56].

Acknowledgments - It is a pleasure to thank Hsiu-Hau Lin, Volker Meden, Jose Riera, and Marcos Rigol for fruitful discussions. We thank Rok Zitko for providing us with NRG data for three dots. E.A. acknowledges support from CNPq and FAPERJ, Brazil. G.B.M. acknowledges support from Research Corporation (Contract No. CC6542). Research at ORNL is sponsored by the Division of Materials Sciences and Engineering, Office of Basic Energy Sciences, U.S. Department of Energy, under contract

DE-AC05-00OR22725 with Oak Ridge National Laboratory, managed and operated by UT-Battelle, LLC. K.A.A., E.D., and F.H.-M. are supported in part by NSF grant DMR-0706020.

- [1] D. Goldhaber-Gordon, H. Shtrikman, D. Mahalu, D. Abusch-Magder, U. Meirav, and M. A. Kastner 1998 *Nature* **391** 156.
- [2] L. Glazman and M. Raikh 1988 *JETP Lett.* **47** 452.
- [3] T. K. Ng and P. A. Lee 1988 *Phys. Rev. Lett.* **61** 1768.
- [4] Y. Meir and P. Lee 1992 *Phys. Rev. Lett.* **68** 2512.
- [5] M. Grobis, I. G. Rau, R. M. Potok, and D. Goldhaber-Gordon, cond-mat/0611480.
- [6] L. Glazman and M. Pustilnik, *Nanophysics: Coherence and Transport*, eds. H. Bouchiat et al. p. 427, Elsevier, 2005.
- [7] M. Pustilnik 2006 *phys. stat. sol. (a)* **203** 1137.
- [8] W. G. van der Wiel, S. D. Franceschi, T. Fujisawa, J. M. Elzerman, S. Tarucha, and L. P. Kouwenhoven 2000 *Science* **289** 2105.
- [9] J. Park, A. N. Pasupathy, J. I. Goldsmith, C. Chang, Y. Yaish, J. R. Petta, M. Rinkoski, J. P. Sethna, H. D. Abruna, and P. L. McEuen . D. C. Ralph 2002 *Nature* **417** 722.
- [10] K. G. Wilson 1975 *Rev. Mod. Phys.* **47** 773.
- [11] H. R. Krishna-murthy, J. W. Wilkins, and K. G. Wilson 1980 *Phys. Rev. B* **21** 1003.
- [12] R. Bulla, T. Costi, and T. Pruschke, *Rev. Mod. Phys.* **80**, 395 (2008).
- [13] S. R. White 1992 *Phys. Rev. Lett.* **69** 2863.
- [14] S. R. White 1993 *Phys. Rev. B* **48** 10345.
- [15] S. R. White and A. E. Feiguin 2004 *Phys. Rev. Lett.* **93** 076401.
- [16] A. Daley, C. Kollath, U. Schollwöck, and G. Vidal 2004 *J. Stat. Mech.: Theory Exp.* P04005.
- [17] U. Schollwöck 2005 *Rev. Mod. Phys.* **77** 259.
- [18] K. Hallberg 2006 *Advances in Physics* **55** 477.
- [19] K. Al-Hassanieh, A. Feiguin, J. Riera, C. A. Büsser, and E. Dagotto 2006 *Phys. Rev. B* **73** 195304.
- [20] G. Schneider and P. Schmitteckert, cond-mat/0601389 .
- [21] C. Karrasch, T. Enss, and V. Meden 2006 *Phys. Rev. B* **73** 235337.
- [22] V. Ferrari, G. Chiappe, E. V. Anda, and M. A. Davidovich 1999 *Phys. Rev. Lett.* **82** 5088.
- [23] C. A. Büsser, E. V. Anda, A. L. Lima, M. A. Davidovich, and G. Chiappe 2000 *Phys. Rev. B* **62** 9907 .
- [24] G. Chiappe and J. A. Verges 2003 *J. Phys.: Condensed Matt.* **15** 8805 .
- [25] C. A. Büsser, A. Moreo, and E. Dagotto 2004 *Phys. Rev. B* **70** 035402 .
- [26] C. A. Büsser et al., unpublished.
- [27] J. E. Gubernatis, J. E. Hirsch, and D. J. Scalapino 1987 *Phys. Rev. B* **35** 8478.
- [28] W. B. Thimm, J. Kroha, and J. von Delft 1999 *Phys. Rev. Lett.* **82** 2143.
- [29] E. S. Sørensen and I. Affleck 2005 *Phys. Rev. Lett.* **94** 086601.
- [30] S. Costamagna, C. Gazza, M. E. Torio, and J. A. Riera 2006 *Phys. Rev. B* **74** 195103.
- [31] L. Borda 2007 *Phys. Rev. B* **75** 041307.
- [32] A. Oguri 1999 *Phys. Rev. B* **59** 12240.
- [33] A. Oguri and A. C. Hewson 2005 *J. Phys. Soc. Jpn.* **74** 988.
- [34] R. Zitko, J. Bonča, A. Ramsak, and T. Rejec 2006 *Phys. Rev. B* **73** 153307.
- [35] R. Zitko and J. Bonča 2007 *Phys. Rev. Lett.* **98** 047203.
- [36] Y. Nisikawa and A. Oguri 2006 *Phys. Rev. B* **73** 125108.
- [37] A. M. Lobos and A. Aligia 2006 *Phys. Rev. B* **74** 165417.
- [38] T. Kuzmenko, K. Kikoin, and Y. Avishai 2003 *Europhys. Lett.* **64** 218.
- [39] C. A. Büsser, G. B. Martins, K. A. Al-Hassanieh, A. Moreo, and E. Dagotto 1004 *Phys. Rev. B* **70** 245303.
- [40] E. V. Anda 1981 *J. Phys. C* **14** 1037.
- [41] W. Metzner 1991 *Phys. Rev. B* **43** 8549.
- [42] M. A. Davidovich, E. V. Anda, C. A. Büsser, and G. Chiappe 2002 *Phys. Rev. B* **65** 233310.

- [43] E. V. Anda, C. A. Büsser, G. Chiappe, and M. A. Davidovich 2002 *Phys. Rev. B* **66** 035307.
- [44] G. B. Martins, C. A. Büsser, K. A. Al-Hassanieh, E. V. Anda, A. Moreo, and E. Dagotto 2006 *Phys. Rev. Lett.* **76** 066802 .
- [45] G. Chiappe, E. Luis, E. V. Anda, and J. A. Verges 2005 *Phys. Rev. B* **71** 241405(R).
- [46] J. M. Aguiar-Hualde, G. Chiappe, E. Louis, and E. V. Anda 2007 *Phys. Rev. B* **76** 155427.
- [47] A. Hewson, *The Kondo Problem to Heavy Fermions* Cambridge University Press, 1993.
- [48] U. Gerland, J. van Delft, T. Costi, and Y. Oreg 2000 *Phys. Rev. Lett.* **84** 3710.
- [49] P. S. Cornaglia and D. R. Grempel 2005 *Phys. Rev. B* **71** 075305.
- [50] R. Berkovits and B. Altshuler, cond-mat/0610466.
- [51] J. Mravlje, A. Ramsak, and T. Rejec 2006 *Phys. Rev. B* **73** 241305(R).
- [52] M. Rontani 2006 *Phys. Rev. Lett.* **97** 076801.
- [53] S. Datta and W. Tian 1997 *Phys. Rev. B* **55** R1914.
- [54] R. Zitko, unpublished results.
- [55] R. Žitko and J. Bonča 2006 *Phys. Rev. B* **73** 035332 .
- [56] E. V. Anda, G. Chiappe, C. A. Büsser, M. A. Davidovich, G. B. Martins, F. Heidrich-Meisner, and E. Dagotto, arXiv:0805.2101.